The Astrophysical Journal, 704:618–628, 2009 October 10 doi:10.1088/0004-637X/704/1/618

UNVEILING THE NATURE OF M94's (NGC4736) OUTER REGION: A PANCHROMATIC PERSPECTIVE

Ignacio Trujillo[1,2,6], Inma Martinez-Valpuesta[1,2], David Martínez-Delgado[1,2,6], Jorge Peñarrubia[3], R. Jay Gabany[4], and Michael Pohlen[5]

[1] Instituto de Astrofísica de Canarias, E-38205, La Laguna, Tenerife, Spain; trujillo@iac.es
[2] Departamento de Astrofísica, Universidad de La Laguna, E-38205 La Laguna, Tenerife, Spain
[3] Institute of Astronomy, University of Cambridge, Madingley Road, Cambridge CB3 0HA, UK
[4] Blackbird Observatory, Mayhill, NM, USA
[5] Cardiff University, School of Physics & Astronomy, Cardiff, CF24 3AA, Wales, UK
Received 2009 May 12; accepted 2009 July 31; published 2009 September 24

ABSTRACT

We have conducted a deep multiwavelength analysis (0.15–160 μm) to study the outer region of the nearby galaxy M94. We show that the non-optical data support the idea that the outskirts of this galaxy are not formed by a closed stellar ring (as traditionally claimed in the literature) but by a spiral arm structure. In this sense, M94 is a good example of a Type III (anti-truncated) disk galaxy having a very bright outer disk. The outer disk of this galaxy contains ∼23% of the total stellar mass budget of the galaxy and contributes ∼10% of the new stars created showing that this region of the galaxy is active. In fact, the specific star formation rate (SFR) of the outer disk (∼0.012 Gyr^{-1}) is a factor of ∼2 larger (i.e., the star formation is more efficient per unit stellar mass) than in the inner disk. We have explored different scenarios to explain the enhanced star formation in the outer disk. We find that the inner disk (if considered as an oval distortion) can dynamically create a spiral arm structure in the outer disk which triggers the observed relatively high SFR as well as an inner ring similar to what is found in this galaxy.

Key words: galaxies: evolution – galaxies: individual (M94, NGC4736) – galaxies: kinematics and dynamics – galaxies: photometry – galaxies: spiral

Online-only material: color figures

1. INTRODUCTION

Recent years have seen a revolution in our understanding of the outskirts of spiral galaxies. On the one hand, ultraviolet (UV) emission in the disk of spiral galaxies has been discovered at very large radii (the so-called XUV disks; Thilker et al. 2005; Gil de Paz et al. 2005; see also Donas et al. 1981), well beyond the optical radius. On the other hand, new studies have challenged the traditional picture of disks of spirals following an exponential radial surface brightness profile (Freeman 1970) down to a large radius where a truncation happens (van der Kruit 1979; van der Kruit & Searle 1981a, 1981b). In fact, recent systematic observations show an unexpected diversity of behaviors in the faintest regions of the surface brightness profiles. Three main categories or types are now established: Type I, in which the disk does in fact show a simple exponential form; Type II, where the inner part of the disk shows an exponential falloff followed by a steeper profile; and Type III, where the inner exponential profile is followed by a shallower, often exponential, profile (Pohlen et al. 2002; Bland-Hawthorn et al. 2005; Erwin et al. 2005, 2008a; Hunter & Elmegreen 2006; Pohlen & Trujillo 2006). There is evidence (Pohlen & Trujillo 2006; Erwin et al. 2008b) that these three types are related with the global morphology of the galaxies (i.e., Type II are more common in later types), implying a suggestive link between the evolutionary patterns followed by the galaxies and the distribution of stars in their outskirts.

Previous observational results suggest that the outer disks provide a direct view of disk assembly. For this reason, several theories have tried to explain the above variety of behaviors in the outer regions of galaxies. Among them we can mention ideas from Yoshii & Sommer-Larsen (1989) who found that to explain Type I profiles the timescales of both viscosity and star formation through the disks should be comparable (see also, Ferguson & Clarke 2001; Slyz et al. 2002). Also, it is possible to find ideas based on star formation thresholds (Kennicutt 1989; Elmegreen & Parravano 1994; Schaye 2004; Elmegreen & Hunter 2006), the maximum angular momentum of the gas that is collapsing to form the disk (van der Kruit 1987; van den Bosch 2001), or secular evolution driven by bars/spiral arms or clumps disruption (Debattista et al. 2006; Bournaud et al. 2007; Roškar et al. 2008; Foyle et al. 2008) to explain the Type II morphology. To justify Type III, tidal stripping caused by minor galaxy mergers (Peñarrubia et al. 2006; Younger et al. 2007), dark matter subhalos bombarding (Kazantzidis et al. 2008), or high eccentricity flyby by a satellite galaxy (Younger et al. 2008) have been proposed. Although these theories qualitative explain the observed behaviors, a quantitative, detailed analysis of the observations that allow us to judge between the different scenarios is missing.

In this paper, we will focus on the nearby galaxy M94 (NGC4736). As we will show through the paper, this galaxy is an example of the brightest anti-truncated (Type III) outer disks that can be found in nearby galaxies. The vicinity of the object (4.66 Mpc; Karachentsev 2005) makes it a perfect candidate to explore in great detail the properties of its outer disk, and consequently, shed some light on the nature of the extended disk phenomenon, particularly, for the most brightest (anti-truncated) outer disk cases.

To achieve this goal, we have compiled data from UV (*Galaxy Evolution Explorer* (*GALEX*)), optical (Sloan Digital Sky Survey (SDSS)), near-infrared (Two Micron All Sky Survey (2MASS)), and infrared (*Spitzer*) to obtain the surface brightness distributions down to faint surface brightness in 17 different filters. The remainder of the paper is organized as follows. In

[6] Ramón y Cajal Fellow.

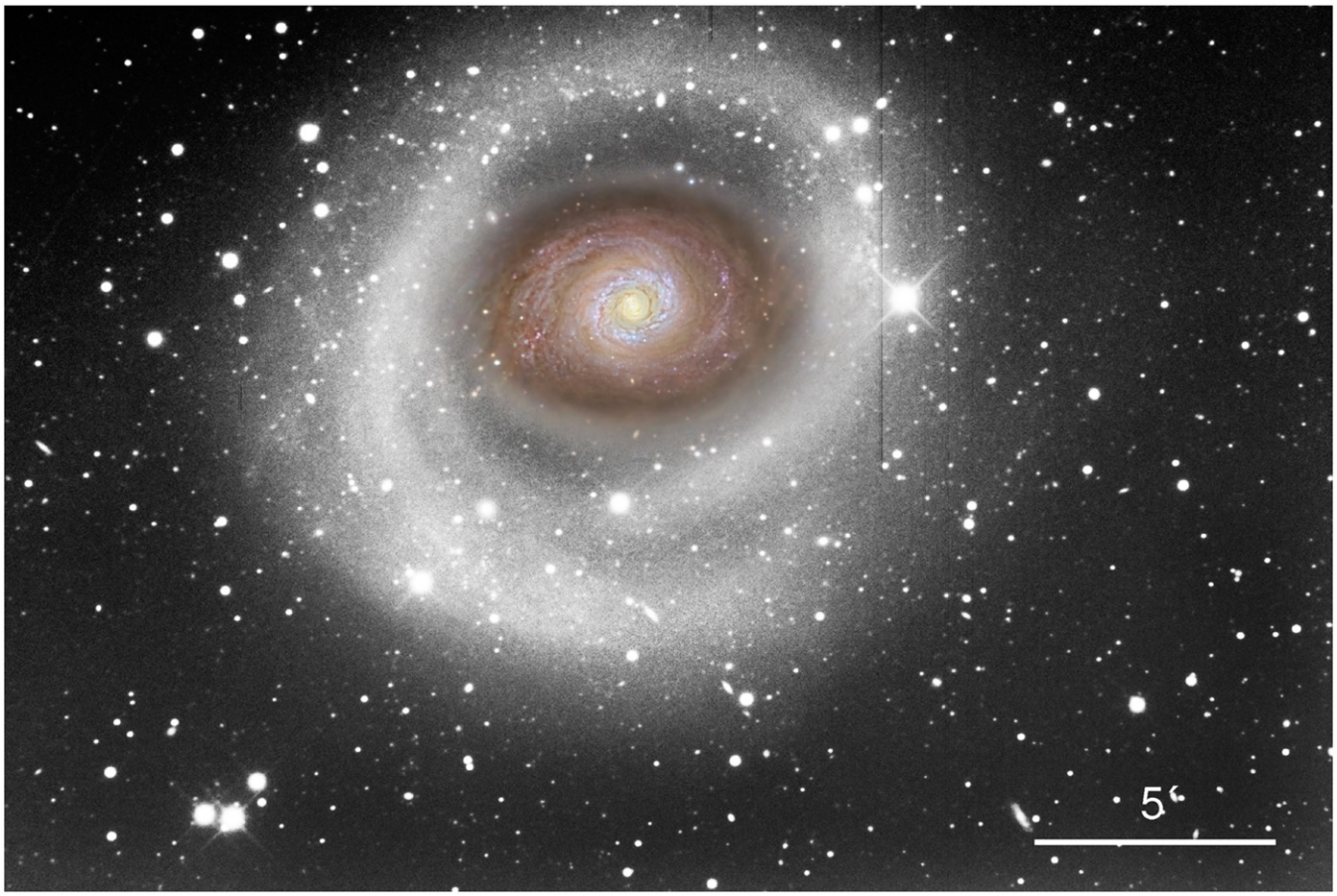

Figure 1. Luminance clear-filter very deep image of M94 (NGC4736) obtained with the BBRO 0.5 m telescope. The total exposure time of the image was 555 minutes. The image size is $27\farcm7 \times 18\farcm2$. North is up and east is left. For illustrative purpose, a color image of the central part of the galaxy obtained with the same telescope has been superimposed on the inner (saturated) disk region of the galaxy. It is worth stressing that the traditional ("textbook") picture of M94 is just what it is shown in color here.

(A color version of this figure is available in the online journal.)

Section 2, we give a brief summary of the structural characteristics of M94. Section 3 contains a detailed description of the data that we have used to conduct our analysis. The dependence with the wavelength of the outer galaxy structure is shown in Section 4. Section 5 shows the surface brightness profiles of the galaxies in 17 different filters from FUV to MIPS 160 μm. The results of our analysis are explained in Section 6. Different formation scenarios are proposed to explain our results in Section 7. Finally, in Section 8 we summarize our main results.

2. M94 (NGC4736) IN A NUTSHELL

M94 is the closest early-type spiral galaxy with low inclination (see Figure 1). It is located in the Canes Venatici I cloud and was classified as (R)SA(r)ab-type according to de Vaucouleurs et al. (1991) and reclassified as (R)SAB(rs)ab-type by Buta et al. (2007). Its total apparent magnitude in the B band is 8.54 mag, its R_{25} is $\sim 337''$ and it is claimed to be at an inclination of 35° (Erwin 2004).

Up to five main regions have been identified in this system according to Bosma et al. (1977): a bulge $R < 15''$ (see also, Beckman et al. 1991), an inner ring of ongoing starburst activity ($R \approx 45''$; van der Kruit 1976), an oval (disk/bar) stellar distribution down to intermediate distance ($R \approx 220''$; Beckman et al. 1991; Shaw et al. 1993; Möllenhoff et al. 1995; Mulder 1995), a zone of low surface brightness (a gap), and what has been traditionally considered as an outer stellar ring around $R \approx 350''$ (see also, Buta 1988; Muñoz-Tuñón et al. 1989). Figure 1 illustrates the different regions of this galaxy as viewed by a very deep exposure obtained by our group (see details in the next section).

M94 is also known for hosting the closest example of a low-ionization nuclear emission-line (LINER) 2 nucleus (see, e.g., Roberts et al. 2001), although the origin of this emission as powered by a low-luminosity active galactic nucleus (LLAGN) is uncertain. Several observations supporting the hypothesis of a non-stellar origin for this emission are the detection of a strong non-thermal radio continuum source at the position of the nucleus (Turner & Ho 1994), the detection in UV using the *Hubble Space Telescope* (*HST*) of two bright point sources in the nuclear region with possible bow shocks resulting from an hypothetical merger of two supermassive blackholes (Maoz et al. 1995), and the detection of a X-ray spectrum dominated by a Seyfert-like power-law continuum (Roberts et al. 1999). On the other hand, favoring the stellar emission hypothesis to explain the LINER emission are the large [Fe II]/Paβ ratio (Larkin et al. 1998), and the Hα (Taniguchi et al. 1996) and FIR luminosities (Smith et al. 1991, 1994).

3. OBSERVATIONS

The analysis conducted in this paper is based on a multiwavelength coverage of the galaxy. Consequently, the data come from a variety of facilities and have been mostly obtained

Figure 2. Panel showing M94 (NGC4736) galaxy through the ultraviolet, optical, and infrared wavelengths. Left panel shows M94 as viewed by the *GALEX* bands (blue: FUV; yellow: NUV). Middle panel shows M94 as viewed by the SDSS bands (blue: *g* band; green: *r* band; red: *i* band). Right panel shows M94 as viewed by the *Spitzer* bands (blue: 3.6 μm; green: 8 μm; red: 24 μm). In all the cases, north is up and east is left. The area shown ($18' \times 15'$) is selected for being the common area covered by the set of facilities used in this work.

(A color version of this figure is available in the online journal.)

from archives. Below follows a brief description of the data collected.

3.1. Deep Optical Luminance Imaging

In order to explore in detail the structural characteristics of the outer region of M94 in the optical regime, we decided to take a very deep exposure of this galaxy (see Figure 1) using the Ritchey–Chrétien 0.5 m telescope of the BlackBird Remote Observatory (BBRO) situated in the Sacramento Mountains (New Mexico, USA). The camera used was a Santa Barbara Instrument Group (SBIG) STL-11100 CCD camera, which has a field of view (FOV) of $27\farcm7 \times 18\farcm2$ and a pixel size of $0\farcs45$. The angular resolution of this image is $\sim 3\farcs4$.

To maximize the photon collection, our imaging consists on multiple deep exposures through a very broad non-infrared clear luminance filter ($3500\ \text{Å} < \lambda < 8500\ \text{Å}$), and a set of red, green, and blue filters from the SGBI custom scientific filters set.[7] The total luminance exposure time allocated to this image was 555 minutes. In addition, to decrease the effect of noise, and consequently increase the detection and enhancing of the faint structures we have applied a Gaussian blur filter (Davies 1990, p. 42; Haralick & Shapiro 1992, Chapter 7). The sigma of the Gaussian kernel used on convolving the images is 1 pixel. This kernel was applied only to the outer regions to reveal more clearly this structure. As shown in a previous work (Martínez-Delgado et al. 2008), the faintest structures reachable with the BBRO telescope using the luminance filter with similar exposure times is $\gtrsim$27.5 mag arcsec^{-2} in the *R* band.

Since we lack a calibration of the optical luminance filter, our image is used only to show the faint structure of the outer disk at these wavelengths.

3.2. GALEX *UV*

The UV observations are obtained from the *GALEX* mission (Martin et al. 2005). In particular, these data were retrieved from the Nearby Galaxy Survey mission (Bianchi et al. 2003a, 2003b; Gil de Paz et al. 2004, 2007). *GALEX* imaging benefits from a large FOV (1.°25 diameter), a very low sky background and high sensitivity. We have used its two UV filters: a far-ultraviolet (FUV) filter centered at 1528 Å (FWHM 269 Å) and a near-ultraviolet (NUV) filter centered at 2271 Å (FWHM 616 Å). The angular resolution of these imaging is $\sim 4\farcs6$, and pixel size is $1\farcs5$. Absolute calibration uncertainties are $\sim$15% in both the FUV and NUV (Dale et al. 2007). An image of M94 (NGC4736) in the UV filters can be seen in the left panel of Figure 2.

3.3. SDSS Optical

Optical data in five bands (u', g', r', i', and z') were obtained from the SDSS (York et al. 2000) archive. SDSS images have a pixel size of $0\farcs396$ and typical angular resolution of $\sim 1''$. Due to the large apparent size of the galaxy, we had to create a mosaic of eight individual SDSS frames ($13\farcm5 \times 9\farcm8$ each) to cover the total galaxy angular extension. An image of the galaxy in the SDSS optical bands can be seen in the central panel of Figure 2.

3.4. 2MASS Near-Infrared

J_s, H, and K_s images were extracted from the 2MASS NASA/IPAC Infrared Science Archive (IRSA). This galaxy is included in the 2MASS Large Galaxy Atlas (Jarrett et al. 2003). This atlas already provides a single image ($20' \times 23\farcm3$) covering this galaxy composed of the individual 2MASS fields. The angular resolution is $\sim 3''$ and the pixel size is $1''$.

3.5. Spitzer *Infrared*

IRAC (3.6 μm, 4.5 μm, 5.8 μm, and 8 μm) bands and MIPS (24 μm, 70 μm, and 160 μm) bands were obtained from the *Spitzer* Legacy program SINGS (Kennicutt et al. 2003). The pixel size is $0\farcs75$ for the IRAC ($24\farcm6 \times 17\farcm9$) mosaics, and $1\farcs5$, $4\farcs5$, and $9''$ for MIPS 24 μm, 70 μm, and 160 μm mosaics, respectively. Calibration uncertainties are $\sim$10% for IRAC data, and 4% (24 μm), 7% (70 μm), 12% (160 μm) for MIPS data (Dale et al. 2007). An image of M94 (NGC4736) in the *Spitzer* infrared filters can be seen in the right panel of Figure 2. The angular resolution of these images is summarized in Table 1.

4. OUTER GALAXY STRUCTURE WAVELENGTH DEPENDENCE

The outer region of M94 (NGC4736) is claimed to be a stellar ring, as mentioned in Section 2. This is in fact the appearance of this structure when observed at the optical wavelengths (see the optical luminance image in Figure 1 and the optical SDSS image in the central panel in Figure 2). The nature of this region, however, seems to be radically different when it is probed both in the UV and in the infrared (see left and right panels in Figure 2).

[7] http://www.sbig.com/products/

Table 1
Data Quality and Galactic Extinction Correction

Band	$\mu_{\rm crit}$(mag arcsec^{-2})	$R_{\rm crit}(")$	PSF FHWM (")	A_λ (mag)
FUV	31.5	550	4.5	0.134
NUV	31.3	650	4.7	0.119
u	28.2	660	1.5	0.093
g	28.2	710	1.2	0.070
r	27.5	730	1.0	0.050
i	27.2	690	1.1	0.037
z	26.7	670	1.0	0.030
J	24.1	205	3.0	0.017
H	23.8	210	2.9	0.010
K	24.3	210	3.0	0.007
3.6 μm	26.6	660	1.7	0.004
4.5 μm	25.8	630	1.9	0.001
5.8 μm	25.0	360	2.0	···
8.0 μm	26.0	415	2.2	···
24 μm	25.5	360	5.5[a]	···
70 μm	23.2	410	15.8[a]	···
160 μm	21.5	450	34.6[a]	···

Notes. Last column, A_λ, is the magnitude correction applied to correct for Galactic extinction (Schlegel et al. 1998) using $E(B-V) = 0.018$ mag.
[a]Values obtained from a Gaussian fit to theoretical PSF models constructed by the Tiny Tim Point Spread Function modeling program (developed for the Spitzer Science Center by John Krist; STScI) to a blackbody source of 50 K temperature (http://ssc.spitzer.caltech.edu/mips/psf.html).

In fact, at these wavelengths, the outer region is better described as an outer disk having spiral arms.

Further support for the outer region being a disk with a spiral arm structure and not a closed stellar ring can be found from the deep H I imaging done by Braun (1995; his Figure 8) and de Blok et al. (2008; their Figure 80). In these figures, a bright spiral arm is seen in the outer disk. This arm, that is not visible in the optical, corresponds to the brightest feature observed in the outer region on the *Spitzer* 24 μm image (see Figure 2) and it is also very clear in the UV imaging. Consequently, the non-optical data strongly point out in the direction of that the outer region of M94 is actually a disk with a spiral arm structure and not a ring as has been traditionally claimed in the literature. In what follows we explore the properties of this outer disk in comparison to the different regions of the galaxy.

5. SURFACE BRIGHTNESS PROFILES

In order to derive surface brightness profiles in a consistent way, we use the same set of ellipticity and position angle (P.A.) in all our bands. Following Pohlen & Trujillo (2006), we explore which value of the ellipticity and P.A. are a good representation of the outer disk. To remove as much as possible potential effects related to star formation and dust extinction, we use the 3.6 μm image as a proxy. Briefly, the method works as follows, we use the IRAF[8] task *ellipse* (STSDAS package) on the sky substracted and masked (from all non-galaxy component) image. The center of the ellipses is fixed by a Gaussian fit to the bright nucleus of the galaxy. We used a logarithmic radial sampling with steps of 0.03 to increase the S/N especially in the outer parts. Iterative 3σ rejection along the ellipse is applied to minimize the influence of cosmic rays or remaining foreground stars. The free ellipse fit (fixed center, free ellipticity, and P.A.) is used to determine the best set of ellipticity and P.A. describing the outer disk. These values are taken at the radius where the mean flux of the best-fitted free ellipse reaches the value of the standard deviation of our background sky. This limit ensures enough S/N to fit a free ellipse but is small enough to be in the radial region dominated by the outer disk.

[8] IRAF is distributed by the National Optical Astronomy Observatories, which is operated by the Association of Universities for Research in Astronomy, Inc., under cooperative agreement with the National Science Foundation.

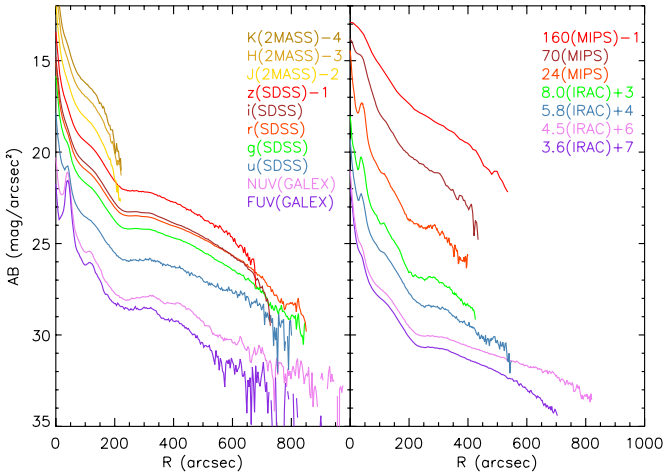

Figure 3. Surface brightness profiles (AB system) of M94 (NGC4736) in 17 bands ranging from the FUV to MIPS 160 μm.
(A color version of this figure is available in the online journal.)

Using 3.6 μm image, we find that the outer isophotes are well described by an ellipticity of 0.14 and a P.A. of 122.°2 (anticlockwise from north). This ellipticity implies an inclination of $\sim$8° for the galaxy, far away from previous reported values of 35° based on the shape of the inner (oval distortion) disk. The P.A. is also different from the one reported previously of 108° (Sofue et al. 1999) for the same reason.

The surface brightness profiles in all the filters were obtained using a task custom-made using IDL. Bright stars were identified and masked. We measured the median intensity and rms along elliptical apertures with fixed ellipticity and P.A. Our code was tested against the IRAF task *ellipse* producing very similar results.

A critical issue for obtaining accurate surface brightness profiles at the low surface brightness levels of the galaxies is the accuracy of the sky substraction. Although the archive data used in this work are sky subtracted, we repeated the "ellipse method" explained in Pohlen & Trujillo (2006) to improve the sky determination. In brief, the idea is to expand the surface brightness estimation using the ellipticity and P.A. obtained from the outer disk. By plotting the flux at these ellipses as a function of radius, it becomes clear at which radial distance the ellipses leave the galaxy and enter the background, flat flux (noise), region (see Figure 2 of Pohlen & Trujillo 2006). The mean value and standard deviation of the fluxes within the above radius and the radius extended by 20% are used as the final sky values. This sky value is subtracted to the original image and the process of estimating the surface brightness is repeated. Our surface brightness estimation (given in the AB system) is shown on Figure 3.

Each image has a critical surface brightness ($\mu_{\rm crit}$) beyond that the reported surface brightness profiles are not reliable. Using SDSS imaging, Pohlen & Trujillo (2006) defined this $\mu_{\rm crit}$ as the value where the profiles obtained by either over- or undersubtracting the sky by $\pm 1\sigma$-sky start to deviate by more than 0.2 mag. This value is 0.54 mag above the limiting surface brightness ($\mu_{\rm lim}$) of the image calculated as the 3σ error of the

sky value determination. Table 1 compiles the set of $\mu_{\rm crit}$ for the different bands used in this work. The surface brightness are corrected for Galactic extinction (Schlegel et al. 1998) using $E(B-V) = 0.018$ mag. No attempt was made to correct the surface brightness measurements for internal extinction, since no unique recipe is available to do this. Consequently, this will introduce an additional uncertainty on the surface brightness estimation. In addition, the galaxy studied here is a fairly face-on system (the measured ellipticity implies an 8° inclination) so the expected correction is only very small. In fact, if we adopt a popular parameterization of the effects of internal extinction (see, e.g., Cho & Park 2009): $A_\lambda = \gamma_\lambda \log_{10}(a/b)$ where γ_λ is a constant that depends on the observed wavelength but which value is ∼1, and a/b is the axis ratio, then in our case, $\log_{10}(1.16) = 0.064$. So the expected corrections are really minor.

Following the estimations of $\mu_{\rm crit}$ we find that, with the exception of the shallow 2MASS near-infrared images (which do not allow us to study the outer disk), we can choose the following outest radius (430″) as a compromise among the different profiles depth. From now onward, consequently, we will divide the galaxy into the following zones: bulge region (0″–75″), inner disk region (75″–200″), and outer disk region (200″–430″).

6. RESULTS

6.1. Surface Brightness Profile Shapes

The observed profiles coupled with the galaxy morphology suggest classifying this galaxy as a Type III (Erwin et al. 2005). In fact, one of the most interesting features of the surface brightness profiles of M94 is the unchanging nature of the global structure of the galaxy from the UV to the far-infrared. This implies that stars of all ages as well as dust are similarly distributed throughout the galaxy structure. The similarity between the UV and FIR profiles is more or less expected as both wavelength ranges are tracing the most active star formation regions of the galaxies. In relation to the optical and NIR data (although we warn that for these last data we lack the information in the outer region) which trace the intermediate-old stellar component, we think that the fact that they also share the shape of the young stellar component implies that the galaxy, globally, is actively forming new stars through all the disk and that this activity has been maintained similarly in the last gigayears. As we will show later in the paper, this scenario is supported by the specific star formation rate (sSFR) distribution of the galaxy which is relatively constant within a factor of 3 through the whole galaxy and by the fact that the gas exponential infall timescales are similar along the galaxy.

An exception is seen for the 70 and 160 μm MIPS bands, where we see the inner star-forming ring is almost invisible. However, that is clearly the effect of the larger point-spread function (PSF) at these wavelengths (cf. Table 1).

One of the most interesting features of the surface brightness profile of M94 is the brightness (∼23.5 mag arcsec^{-2} in r' band) at which the outer disk appears. Normally, for Type III galaxies, the break occurs at faintest surface brightness. For example, Pohlen & Trujillo (2006) find a typical surface brightness of ∼24.7 ± 0.8 mag arcsec^{-2} in the r' band, whereas Erwin et al. (2008a) find ∼24.2 ± 0.5 mag arcsec^{-2} in the R band. This makes M94, in comparison, a Type III galaxy having an outer disk on the very bright side. However, M94 is not an unique example within the family of Type III objects, in fact, it is possible to find other galaxies with similar characteristics. For example, M77 (NGC1068) is strikingly similar to M94 (see its profile on Pohlen & Trujillo 2006). In the case of M77, the outer disk starts at ∼23 mag arcsec^{-2}, and morphologically also, both have similar features. For this reason, we think that both of these two galaxies could be considered as examples of Type III galaxies having the brightest (<23.5 mag arcsec^{-2} in r' band) anti-truncated outer disks. However, a note of caution should be stated about the type of the galaxy M94. The Type III classification is based on the assumption (following the traditional picture of this galaxy) that the inner region (75″–200″) is a true disk. If this region is, however, considered as an oval distortion (i.e., a structure with a bar-like nature and not a real disk), then the genuine disk of the galaxy is the outer region (>200″) and the galaxy should be better considered as a Type I.

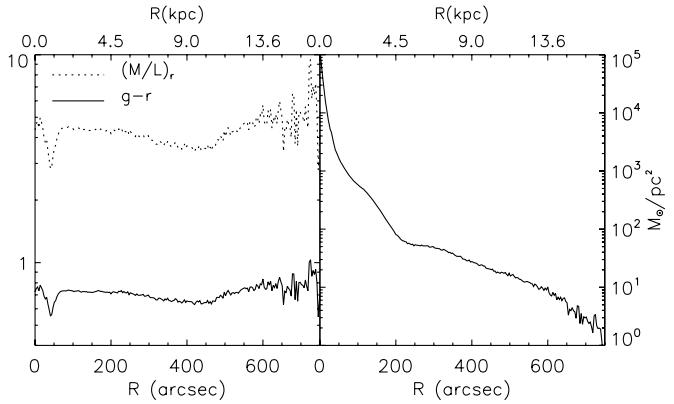

Figure 4. Left panel: $(g-r)$ color and $(M/L)_r$ profiles of M94. Right panel: stellar mass density profile of M94 (NGC4736) obtained using the r-band profile and $(M/L)_r$ from the $(g-r)$ color following the prescription given by Bell et al. (2003).

6.2. Stellar Mass Surface Density Profile

At any given wavelength, it can be shown that the surface brightness profiles μ_λ can be converted into stellar mass surface density profiles as follows:

$$\log(M/(M_\odot\,{\rm pc}^2)) = \log(M/L)_\lambda - 0.4(\mu_\lambda - m_{{\rm abs},\odot,\lambda}) + 8.629 \quad (1)$$

with $(M/L)_\lambda$ the stellar mass-to-light ratio in solar units and $m_{{\rm abs},\odot,\lambda}$ the absolute magnitude of the Sun at a given wavelength λ. Lacking a deep near-infrared image, we have chosen the SDSS r band to estimate the M/L ratio. This band is selected because it is the reddest of the deepest SDSS bands. To estimate the $(M/L)_r$ ratio, we have used the $(g-r)$ color following the prescription given by Bell et al. (2003). We add 0.15 dex to the M/L obtained in Bell et al. (2003) to normalize the predicted M/L to a Salpeter (1955) initial mass function (IMF). The $(g-r)$ color profile, the $(M/L)_r$, and the stellar mass density profile are shown in Figure 4. The minimum observed both in color and $(M/L)_r$ is associated with the nuclear stellar ring. The shape of the stellar mass density profile is very similar to the shape of the reddest (stellar origin) surface brightness profiles we have. The stellar mass density at which the outer disk starts is $\sim 60\,M_\odot$ pc^{-2}. As expected due to M94's bright outer disk, this value is higher than the mean value measured for late-type Type III galaxies ($\sim 10\,M_\odot$ pc^{-2}; Bakos et al. 2008).

Using the stellar mass density profile based on colors, one can calculate a rough estimate of the total stellar mass of the galaxy:

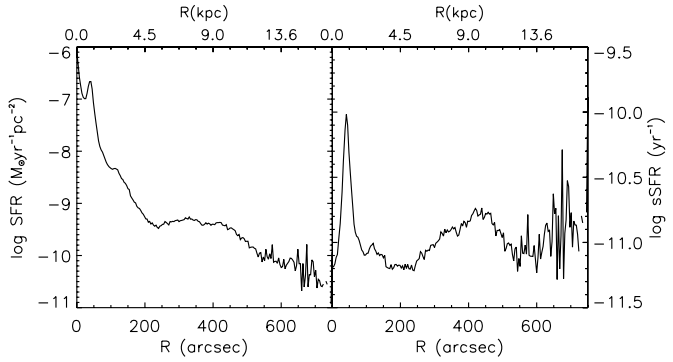

Figure 5. Left panel: SFR profile of M94. Right panel: sSFR profile of M94.

$\sim 6.5 \times 10^{10}\, M_\odot$. In each of the galaxy regions,[9] the amount of stellar mass we measure is bulge region ($3.2 \times 10^{10}\, M_\odot$), inner disk region ($1.7 \times 10^{10}\, M_\odot$), and outer disk region ($1.5 \times 10^{10}\, M_\odot$). Due to the significant brightness of the outer disk, its contribution to the total stellar mass budget of the galaxy is quite significant ($\sim$23%). This is a factor of $\sim$2 larger than the average late-type Type III outer disk (Bakos et al. 2008).

6.3. Star Formation Rates

To assess the origin of the outer disk structure, a key element is to measure its star formation rate (SFR). This value can give us clues on whether this region of the galaxy is still forming (i.e., creating new stars) or whether it is an old structure. Following Muñoz-Mateos et al. (2007), the SFR can be computed from the apparent magnitude (corrected for internal extinction) in the FUV (AB system) using the calibration given by Kennicutt (1998)

$$\log(\mathrm{SFR})(M_\odot\ \mathrm{yr}^{-1}) = 2\log d(\mathrm{pc}) - 0.4\ \mathrm{FUV}\ - 9.216. \quad (2)$$

This can be transformed to a SFR per surface area as follows:

$$\log(\mathrm{SFR}_\mu)(M_\odot\ \mathrm{yr}^{-1}\ \mathrm{pc}^{-2}) = -0.4\mu_{\mathrm{FUV}} + 1.413. \quad (3)$$

To estimate the internal extinction $A_{\mathrm{FUV,in}}$ in the FUV, we follow the empirical relation between the TIR-to-FUV ratio (i.e., the total luminosity in the infrared over the luminosity in the FUV), $\log(F_{\mathrm{TIR}}/F_{\mathrm{FUV}})$ and the observed (FUV–NUV) color derived by Boissier et al. (2007). Once $\log(F_{\mathrm{TIR}}/F_{\mathrm{FUV}})$ is obtained, the attenuation profiles are computed using the fit of Buat et al. (2005)

$$A_{\mathrm{FUV,in}} = -0.0333X^3 + 0.3522X^2 + 1.1960X + 0.4967 \quad (4)$$

with $X = \log(F_{\mathrm{TIR}}/F_{\mathrm{FUV}})$. The median value of $A_{\mathrm{FUV,in}}$ within the inner 430″ is 1.7 mag. This translates (using $A_K = 0.0465A_{\mathrm{FUV}}$; Muñoz-Mateos et al. 2007) to an inner median extinction in the K-band profile of 0.079 mag.

Using Equation (2), we can estimate the total SFR of the galaxies as well as the SFR at the different components. We find that the total SFR for M94 is $1.04\, M_\odot\ \mathrm{yr}^{-1}$ which is distributed across the different regions of the galaxy as follows: bulge ($0.75\, M_\odot\ \mathrm{yr}^{-1}$), inner disk ($0.14\, M_\odot\ \mathrm{yr}^{-1}$), and outer disk ($0.15\, M_\odot\ \mathrm{yr}^{-1}$). The amount of stars the outer disk is forming is comparable to the inner disk and it is a significant (10%–15%) fraction of the total SFR of the galaxy. This clearly shows, that at least for M94, the outer disk is a very active region of the galaxy. This activity is directly visible when looking at the UV and IR images shown in Figure 2, where the unobscured young stars as well as the hot dust are clearly seen in form of spiral arms in the outer region of the galaxy.

[9] We would like to emphasize that the term regions used here (as well as in the rest of the paper) should not be confused with the actual components of the galaxy (i.e., bulge, inner disk, outer disk, etc.). This distinction is relevant when estimating quantities like the amount of mass since the real components of the galaxy can indeed overlap.

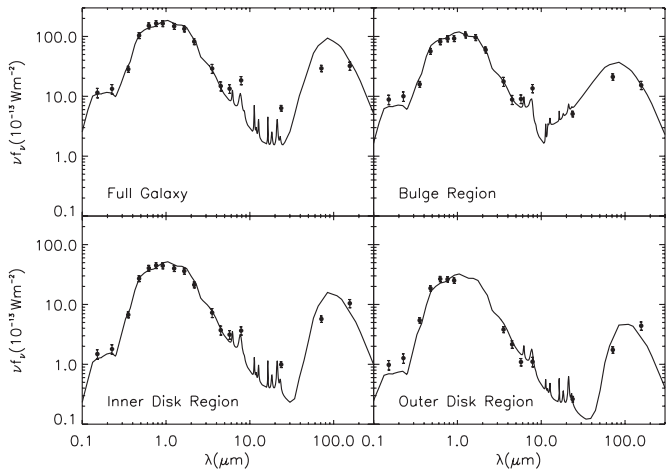

Figure 6. M94 (NGC4736) galaxy 0.15–160 μm SEDs of the total galaxy, its bulge, inner disk, and outer disk regions. The solid points are the observed data and the line is the best-fit model.

Another important parameter to measure is the sSFR, i.e., the amount of star formation per unit stellar mass. This value informs about the efficiency of the star formation in the different regions of the galaxies. The sSFR can be derived from the combination of Equations (1) and (3) to give

$$\log(\mathrm{sSFR})(\mathrm{yr}^{-1}) = -0.4(\mathrm{FUV} - m_\lambda) - \log(M/L_\lambda) - 0.4m_{\mathrm{abs},\odot,\lambda} - 7.216. \quad (5)$$

Both SFR and sSFR radial distributions are plotted in Figure 5. Our estimates agree very well by those produced by Boissier et al. (2007) for the SFR density (their Figure 9.39) of this galaxy: $\sim 10^{-8}\, M_\odot\ \mathrm{pc}^{-2}\ \mathrm{yr}^{-1}$ at 50″ (bulge), $\sim 5 \times 10^{-9}\, M_\odot\ \mathrm{pc}^{-2}\ \mathrm{yr}^{-1}$ at 150″ (inner disk), and $\sim 4 \times 10^{-10}\, M_\odot\ \mathrm{pc}^{-2}\ \mathrm{yr}^{-1}$ at 300″ (outer disk). Muñoz-Mateos et al. (2007) have noted that nearby spirals show a slightly positive increase of the sSFR from inside-out. This result also applies in the particular case of M94, where we find that the outer disk has a larger sSFR ($\sim$0.012 Gyr^{-1}) than the inner disk ($\sim$0.006 Gyr^{-1}). In other words, per unit stellar mass, the outer disk is more active (efficient) forming stars.

6.4. Spectral Energy Distributions

Using the fluxes obtained in the 17 filter bands, we have created the spectral energy distributions (SEDs) ranging from 0.15 to 160 μm in the different regions of the galaxy (see Table 2). The SEDs across the galaxy are shown in Figure 6.

To extract some relevant physical parameters from the SEDs, we have used synthetic templates computed with the code GRASIL (Silva et al. 1998). This code couples the spectral (and chemical) evolution of stellar populations with the radiative transfer through a dusty interstellar medium. Consequently, the models consistently account for the emission from stars as well as absorption and emission from dust in galaxies. GRASIL allows the variation of a large set of free parameters but here we

Table 2
Ultraviolet, Optical, Near-infrared, Infrared Flux Densities

Rad. Ran. (″)	FUV (Jy)	NUV (Jy)	u (Jy)	g (Jy)	r (Jy)	i (Jy)	z (Jy)	J (Jy)	H (Jy)	K_S (Jy)	3.6 (Jy)	4.5 (Jy)	5.8 (Jy)	8 (Jy)	24 (Jy)	70 (Jy)	160 (Jy)
0–75	0.045	0.076	0.19	0.90	1.70	2.33	2.82	4.44	5.28	4.32	2.09	1.32	1.73	3.57	4.02	>50.29	>79.72
75–200	0.008	0.014	0.08	0.43	0.84	1.14	1.35	1.67	1.99	1.54	0.86	0.56	0.60	0.96	0.78	<13.62	<54.33
200–430	0.005	0.010	0.06	0.30	0.55	0.67	0.77	···	···	···	0.45	0.32	0.21	0.29	0.21	<4.15	<22.88
0–430	0.058	0.100	0.34	1.65	3.14	4.20	5.01	>6.18	>7.37	>5.94	3.44	2.22	2.56	4.85	5.02	69.85	167.34

Table 3
Best-fit Parameters and Derived Quantities of the SED GRASIL Models

Rad. Ran. (″)	τ_b (Gyr)	$M_{\rm inf}$ ($10^{10}\ M_\odot$)	$\nu_{\rm sch}$ (Gyr^{-1})	$M_{\rm mol}/M_{\rm gas}$	$t_{\rm esc}$ (Gyr)	$M_{\rm MC}$ ($10^6\ M_\odot$)	SFR ($M_\odot$ yr^{-1})	$\tau_{\rm MC}$	$M_{\rm gas}$ ($10^8\ M_\odot$)	$M_\star$ ($10^{10}\ M_\odot$)
0–75	3.7 ± 0.9	3.1 ± 0.5	2.4 ± 0.8	0.49 ± 0.25	0.030 ± 0.017	1.3 ± 0.7	0.64 ± 0.40	60 ± 14	2.63 ± 0.62	2.75 ± 0.45
75–200	2.8 ± 0.9	1.4 ± 0.3	2.1 ± 1.0	0.52 ± 0.24	0.051 ± 0.023	6.9 ± 2.9	0.19 ± 0.18	346 ± 98	0.84 ± 0.31	1.27 ± 0.30
200–430	2.2 ± 0.6	1.0 ± 0.1	2.3 ± 0.8	0.71 ± 0.14	0.032 ± 0.009	8.9 ± 1.3	0.07 ± 0.10	486 ± 12	0.28 ± 0.26	0.86 ± 0.62
0–430	3.9 ± 1.1	4.8 ± 0.8	2.3 ± 0.8	0.49 ± 0.25	0.031 ± 0.019	4.4 ± 3.4	1.07 ± 0.62	205 ± 121	4.50 ± 1.00	4.22 ± 0.63

concentrate only in the small subset that mostly affect the shape of the SED (Panuzzo et al. 2007). We describe briefly which parameters were left to change during the fitting of the SEDs (see Silva et al. 1998 for a detailed description of the code) as follows.

1. Total infall mass, $M_{\rm inf}$. This is the amount of primordial gas that has infalled to form the galaxy. We have allowed the following range of variation depending on the region of the galaxy which is fitted: bulge ((0.8–5) $\times$ 10^{10} $M_\odot$), inner disk ((0.6–3) $\times$ 10^{10} $M_\odot$), outer disk ((0.6–3) $\times$ 10^{10} $M_\odot$), and the full galaxy ((1–7) $\times$ 10^{10} $M_\odot$).
2. Exponential infall timescale, τ_b. Gas is assumed to be continuously infalling at a rate proportional to $\exp(-t/\tau_b)$. τ_b was allowed to change from 0.1 to 10 Gyr.
3. Efficiency of Schmidt-type law, ν. The SFR is assumed in GRASIL to follow a Schmidt-type law of the form $\mathrm{SFR}(t) = \nu M_g(t)^k$, where M_g is the gas mass at any time, k is the exponent of the Schmidt law which we fixed to 1, and ν is the free efficiency parameter varying from 10^{-3} to 4.
4. Fraction of molecular mass to total gas mass ($M_{\rm mol}/M_{\rm gas}$). We allow this parameter to range from 0.1 to 0.99.
5. The escape timescale of newly born stars from their parent molecular clouds, $t_{\rm esc}$. We let this vary from 10^{-3} to 10^{-1} Gyr.
6. The mass of the molecular clouds, $M_{\rm MC}$. The mass of the molecular clouds together with the radii of the molecular clouds is related to the optical depth of the molecular clouds, $\tau_{\rm MC} \propto M_{\rm MC}/r_{\rm MC}^2$. We fixed $r_{\rm MC} = 14$ pc and let $M_{\rm MC}$ vary from 10^3 to 10^7 $M_\odot$.

To allow a comparison with other works the adopted IMF is a Salpeter IMF in the mass range from 0.1 to 100 $M_\odot$. Due to the low inclination of our galaxy, we use the output of the code with zero inclination. We assume that the galaxy has a present age of 13 Gyr.

For the SED of each region, we have computed the minimum χ^2. Due to the large number of free parameters (six in our case), we have avoided a brute force approach that implies to compute a large set of templates. For example, assuming that 10 values per parameter are desired, $10^{N_{\rm par}}$ templates should be created. In current powerful desktops every GRASIL template takes $\sim$30 s to be computed. Consequently, the amount of time required in a brute force approach is prohibitive. To overcome this difficulty, we have applied a Markov chain Monte Carlo technique based on the Metropolis algorithm (Metropolis et al. 1953; Neal 1993). The details of the code that we have used are in Asensio Ramos et al. (2007).

The best-fit parameters together with the 1σ error are shown in Table 3. Together with these values, GRASIL also provides the present SFR and the optical depth of molecular cloud at 1 μm $\tau_{\rm MC}$ and the amount of mass in gas and stars.

We can conduct now a comparison between the stellar mass obtained using the $(g-r)$ color and the ones obtained using the GRASIL code. Comparing the stellar mass determined with GRASIL with the ones derived in Section 6.2, following Bell et al. (2003), we find them systematically ($\sim$0.7) lower. However, it is worth stressing that within the error bars both estimations agree. From the above comparison, we think it is safe saying that the amount of stellar mass contained within the different regions of the galaxy is as follows: ($2.8 < M_\star < 3.2$) $\times$ 10^{10} $M_\odot$ (bulge), ($1.3 < M_\star < 1.7$) $\times$ 10^{10} $M_\odot$ (inner disk), ($0.9 < M_\star < 1.5$) $\times$ 10^{10} $M_\odot$ (outer disk), and ($4.2 < M_\star < 6.5$) $\times$ 10^{10} $M_\odot$ (total). In relation to the SFR, we find that GRASIL and the prescription presented in Muñoz-Mateos et al. (2007) agree very well within the error bars.

The GRASIL prediction in relation to the amount of present gas (i.e., not transformed into stars) in the different regions of the galaxy can be also compared with the recent measurements of H I (Walter et al. 2008). These authors find a total amount of gas of 4 $\times$ 10^8 $M_\odot$ for M94. This number is in excellent agreement with the GRASIL prediction (4.5 ± 1.0) $\times$ 10^8 $M_\odot$.

From the GRASIL results one can extract the following information. (1) The efficiency of the star formation, as characterized by the ν parameter is very similar through the whole structure of the galaxy, with no significant changes from the bulge to the outer disk. (2) The mass of the typical molecular clouds where the star formation is taking place seems, however, to be much smaller in the inner region of the galaxy than in the outer region. This could be related to the much more violent conditions (influence of the active nucleus) close to the center of the galaxy preventing the formation of massive molecular clouds. (3) The exponential infall timescale of the gas seems to vary also across the galaxy. The gas appears to take more time to be deposited in the bulge than what requires to be placed in the outer disk. This could be understood if the gas requires, as expected, a

large loss of angular momentum to feed the bulge than the inner disk.

7. ORIGIN OF THE OUTER DISK

In the following, we will address the origin of M94's bright outer star-forming disk. We will explore the two obvious possibilities of it having an external versus internal origin.

7.1. Merger Origin

It has been proposed (Peñarrubia et al. 2006) that extended galactic disks can be form by a tidally disrupted dwarf galaxy in prograde orbit that is coplanar with the host galaxy disk. As a result of this merging, the stellar debris ends up resettling into an extended exponential disk in dynamical equilibrium. Depending on the mass of the satellite, orbit eccentricity and inclination, the stellar debris exhibit a rotation that could range from 30–50 km s^{-1} lower than the host circular velocity up to a factor of ∼2 smaller.

Favoring a merger origin for the outer disk of M94 is the fact that its rotation curve is declining from the inner region (∼3 kpc) to the outer region (∼9 kpc) by ∼30% (Mulder 1995; de Blok et al. 2008). However, a common concern with the merging scenario (particularly if the merger has a large mass ratio) is the possibility that the accretion destroys the inner disk (Hopkins et al. 2009). In our case, the outer disk of M94 contains a large fraction (∼23%) of the total mass of the galaxy. If all the outer disk were entirely the result of a disrupted dwarf the implied merger ratio would be as high as 1:4.

Another problem with the merger scenario, if we want to explain entirely the outer region of M94 as a tidally disrupted satellite, is the very different ellipticity the inner disk and the outer region has. In the merging hypothesis, the ellipticities of both components can be interpreted as a reflect of the different inclination they have. In fact, transforming the observed ellipticities to inclinations, we find that the inner region will have an inclination of ∼35° whether the outer disk will have only ∼8°. Merging simulations of massive satellites with disk galaxies whereas the disk survived the encounter only found a maximum tilt of ∼7° for the outer regions (Velázquez & White 1999). This is much smaller than what is observed for this galaxy.

Even in the case that the origin of the outer region of M94 could not be explained by a major merger it could be well the case that an interaction of M94 with another galaxy could be the responsible of triggering both the star formation we see in this part of the galaxy as well as the many morphological structures this galaxy has inner ring, inner disk/oval distortion, gap, outer spiral arms, etc. The interaction possibility is, however, disfavored by the observations. Although M94 is the main member of the Canes Venatici I Group, it seems unlikely that it has suffered any interaction with another member of that group recently. In fact, such group has been found to be only weakly gravitationally bound. Moreover, most of the galaxies in this group appear to be moving with the expansion of the universe, which will prevent nearby (repeated) encounters affecting M94 (Karachentsev et al. 2003).

7.2. Secular Evolution

We also explore whether the plethora of structures we see in M94 as well as the enhanced star formation in its periphery could be created assuming a perturbation of internal (secular) origin. It is well known that bars can be produced via dynamical instabilities in galactic disks. A particular form of bars is what is known as oval distortion which are weak bars also called "fat bars" that often resemble normal slightly inclined disk having even spiral arms (see, e.g., Jogee et al. 2002). As mentioned in Section 2, the inner disk of M94 has been sometimes considered as an oval distortion more than a truly inclined disk (Kormendy & Norman 1979). This seems to be a reasonable hypothesis since the inclination of the galaxy, as derived in the UV and IR imaging for the outer disk, is lower than what it would be derived from the shape of the inner disk. It is worth stressing that this conclusion suggesting that the inner region of M94 is an oval distortion more than an truly inclined disk cannot firmly established on the basis of the optical images alone (which were the main source of information used in previous works), but, both the UV and IR images presented in this paper clearly show that there is a continuation in the spiral arms from the inner (oval) region to the outer disk. If both structures were decoupled, as suggested by the apparent different inclination and explained in the merger scenario, this prolongation of the spiral arms would be extremely unlikely. Under the hypothesis that the inner region is an oval distortion the problem with the different inclinations among the inner and the outer disk of M94 is solved since the oval distortion is not inclined but has a different ellipticity than the outer disk because is intrinsically oval and not circular.

If the inner region is an oval distortion, this structure could be a serious candidate to explain the spiral arm structure we see in the outer disk (Binney & Tremaine 1987, and references therein), and consequently to be the ultimate responsible of the enhanced star formation we measure in this part of the galaxy. Oval distortions are known to create spiral arms that can be sustained for long time in isolated galaxies (e.g., Lindblad 1960; Toomre 1969; Sanders & Huntley 1976; Athanassoula 1980). In fact, oval distortions have been considered as important as bars when considering the secular evolution of a disk galaxy (Kormendy & Kennicutt 2004).

We have created a toy model to explore whether the observed oval distortion can produce spiral arms similar to what we see in the outer disk. Our simple model is composed of a bulge, an oval distortion, an outer disk, and a dark matter halo. To characterize the different components of the galaxy, we use different analytical formulae that we fit to the stellar mass density profile in order to have realistic parameters (see Figure 7). Considering the oval distortion as a very mild bar, we use the analytical formula by Ferrers (1877) to describe it

$$\rho = \begin{cases} \frac{15}{8}\frac{M_{\rm od}}{\pi abc}(1-m^2)^1, & m \leqslant 1 \\ 0, & m \geqslant 1, \end{cases} \quad (6)$$

where $m^2 = \frac{x^2}{a^2} + \frac{y^2}{b^2} + \frac{z^2}{c^2}$, and a is the major axis, b is the minor, and c is the vertical axis, taken here as 500 pc, with $a > b > c$. This bar model is very popular in the literature (see, e.g., Sanders & Tubbs 1980; Papayannopoulos & Petrou 1983; Schwarz 1985; Athanassoula 1992; Patsis 2005, etc.). From the fit to the stellar surface mass density we obtain $a = 4.9$ kpc, $b = 4.1$ kpc, and a total mass for the oval distortion equal to $M_{\rm od} = 1.3 \times 10^{10} M_{\odot}$.

The remaining components of the galaxy (the bulge, the outer disk, and the dark matter halo) have been modeled using the Miyamoto & Nagai (1975) analytical models. The Miyamoto–Nagai potential is described by the equation

$$\Phi_M(R,z) = -\frac{GM}{\sqrt{R^2 + (a + \sqrt{z^2 + b^2})^2}}. \quad (7)$$

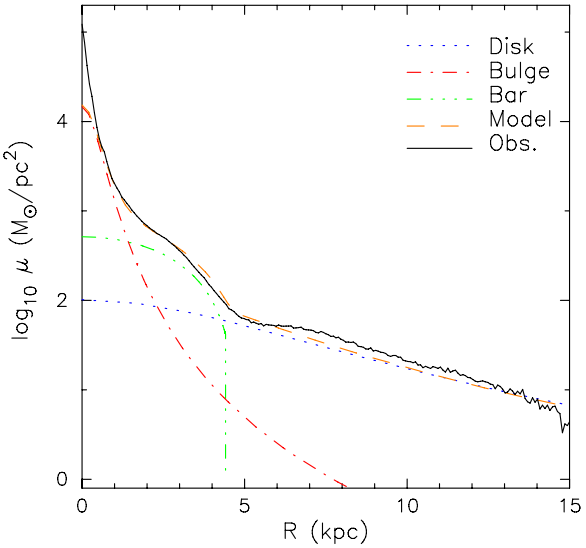

Figure 7. Fit to the surface density profile (shown in Figure 4) using different analytical components. The oval distortion (inner disk) is modeled with a Ferrers bar with $n = 1$. The bulge, outer disk, and halo are fitted using Miyamoto–Nagai models.

(A color version of this figure is available in the online journal.)

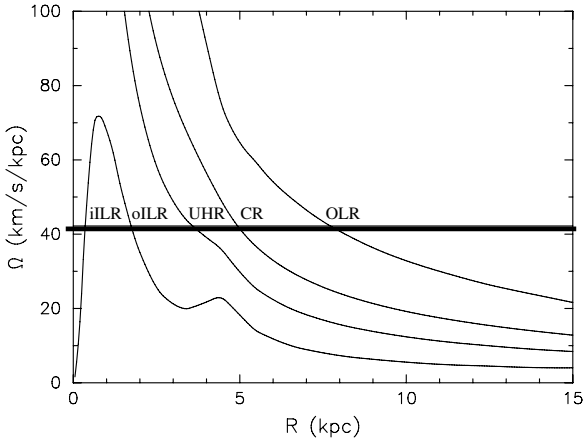

Figure 8. Angular frequency of the proposed model. The solid horizontal line is the pattern speed chosen in this paper.

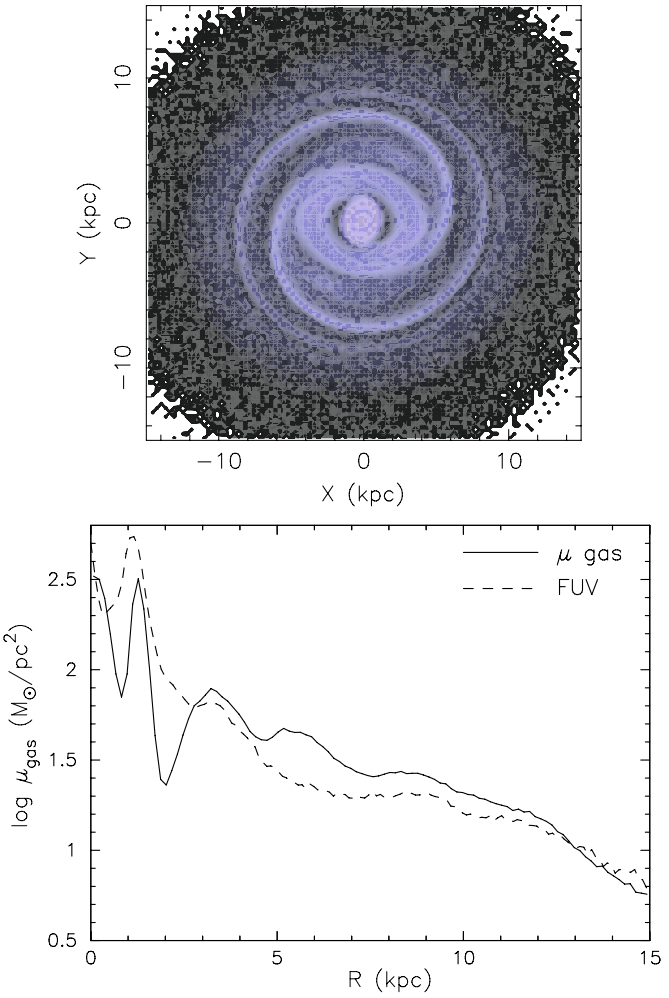

Figure 9. Left panel: snapshot of the SPH simulation showing the spiral arms as a response to the inner oval distortion. Right panel: the solid line shows the gas surface density profile of our model. The different peaks represent the response of the gas to the dynamical effect of the oval distortion. The dashed line shows the FUV surface brightness (i.e., a good proxy to the recent star formation) scaled to fit in the plot.

(A color version of this figure is available in the online journal.)

The parameters retrieved from the fit to the stellar mass surface density are bulge ($M = 2.0 \times 10^{10}\ M_{\odot}$, $a = 0.05$ kpc, and $b = 0.6$ kpc), outer disk ($M = 2.8 \times 10^{10}\ M_{\odot}$, $a = 6.5$ kpc, and $b = 0.5$ kpc), and halo ($M = 20.0 \times 10^{10}\ M_{\odot}$, $a = 0.0$ kpc, and $b = 30$ kpc). Note that the outer disk in this model has a factor of ∼2 more stellar mass than what we have measured before using the outer region (200″–430″) of the stellar mass profile. This is explained because in the model the stellar mass density profile is extrapolated in- and outward, to zero and infinity, respectively. Once the galactic potential is set, we can start running a simulation and see how a gaseous disk responds to the potential. Before doing this, we can use the linear approximation to calculate the angular frequency, and therefore estimate the radii of the main resonances (Figure 8) associated with the gravitational potential we have created. This is important for this galaxy since several resonant structures like the inner ring are observed.

One of the key issues when considering bars, or oval distortions, and their corresponding resonances is the pattern speed, i.e., how fast the bar rotates as a solid body. The pattern speed determines many different structures, such as the radii of the different resonant rings, or their actual existence. In the case of our study, the variation of the pattern speed also determines the appearance of the spiral arms and their shape. A precise study of the spiral arms and their origin (Romero-Gómez et al. 2007) establishes that when increasing the pattern speed in a given barred model, the spiral arms become more tightly wounded.

Several pattern speeds have been proposed to explain different features in M94. We started with $\Omega_p = 56$ km s^{-1} kpc^{-1} proposed by Mulder & Combes (1996) and decreased this value down to $\Omega_p = 30$ km s^{-1} kpc^{-1}. We found that a model that is able to reproduce the shape of the outer spiral arms as well as the inner ring of the galaxy has $\Omega_p = 38$ km s^{-1} kpc^{-1}. This number agrees nicely with previous studies, such as Waller et al. (2001), where they studied the central part of the galaxy and obtained $\Omega_p = 35$ km s^{-1} kpc^{-1}. With the pattern speed that we are using, $R_{\rm CR} = 5.2$ kpc, and consequently $R_{\rm CR}/R_{\rm bar} = 1.04$. In that sense, the oval distortion that we have created would be considered as a fast bar (Aguerri et al. 2003). In addition, our pattern speed produces an inner ring at a radius of ∼1 kpc, at the same distance than the one observed.

Once the gravitational potential and the pattern speed are fixed, we run our simulation to explore the response on a pure gas

disk. We use the code FTM 4.4 (updated version) from Heller & Shlosman (1994), which allow us to study the dynamical response of the gas based on smoothed particle hydrodynamics (SPH). We use 150,000 collisional particles to simulate the gas, isothermal and non self-gravitating. Initially, the gaseous particles are distributed following a Miyamoto–Nagai density distribution. In Figure 9, left panel, we show a snapshot of our simulation showing clearly the spiral arms, as a result of the oval distortion. In addition, the inner ring that is observed in the real galaxy can be seen. To make a more quantitative comparison of our toy model with the observations, in Figure 9, right panel, we compare the density profile of the gas in our simulation with the FUV surface brightness profile. The peaks on the FUV profile represent the places where the star formation is enhanced. We can see that there is a reasonable agreement between the peaks in the FUV and the position of the peaks where the density of the gas in the model is higher.

According to our simulation, if the oval distortion survives for long time (Athanassoula & Misiriotis 2002; Martinez-Valpuesta et al. 2006), the spiral arm and the ring will also survive. However, a slow secular evolution is expected in the radius of the oval structure and the pattern speed. In addition, we should take into account the slowly consumption of the gas by the star formation (which could be somehow counterbalance by the new gas infall) that will also decrease the amount of gas in the spiral arms and oval distortion.

In a forthcoming paper (I. Martínez-Valpuesta et al. 2010, in preparation), we plan to increase the resolution of our hydrodynamical simulation to explore in more detail the inner region of the galaxy. In particular, we will explore the velocity shear field of the galaxy to probe whether the dynamics linked to the oval distortion can help to explain the GRASIL findings in relation to the efficiency, molecular cloud mass, and infall timescale found from the stellar population analysis. Our aim is to find a consistent model able to reproduce at the same time the new H I kinematic data (de Blok et al. 2008) in the outer region.

8. CONCLUSIONS

M94 is the closest example of an early-type spiral galaxy with low inclination. It has been traditionally considered (due to its optical appearance) as a galaxy with a bright outer ring surrounding its disk. The multiwavelength analysis that we have conducted in this paper shows that this view is incorrect. Observed in the UV and in the IR, the galaxy reveals that its outer region has a disk with a spiral arms structure nature. This outer disk is very active forming stars and contains ∼23% of the total mass of the galaxy. We have explored what is enhancing this star formation activity in the galaxy periphery and find that a likely candidate is the dynamical effect of the inner oval distortion on the rest of the galaxy. Although an external origin of the extended disk (e.g., due to the accretion of a satellite galaxy) cannot be ruled out with the existing data, the oval distortion hypothesis explains more naturally the existence of an inner ring and the enhanced star formation activity in the outer disk of M94. In addition, it is likely that the flux of gas that the oval distortion produces toward the center of the galaxy would be related to the active nature of the bulge of this galaxy.

We are happy to thank Jose Antonio Acosta Pulido, Juan Carlos Muñoz-Mateos, Armando Gil de Paz, and Olga Vega for their interesting comments on different aspects of this work. Thanks are also given to Andres Asensio Ramos and Jose Alberto Rubiño Martín for their help on using their Markov chain algorithm, and to Yoshiaki Sofue. We also thank to the THINGS team (especially Erwin de Blok) for providing us with kinematical data of M94. We also acknowledge the detailed review of the manuscript done by the referee. I.T. and D.M.-G. acknowledge support from the Ramón y Cajal Program financed by the Spanish Government.

REFERENCES

Aguerri, J. A. L., Debattista, V. P., & Corsini, E. M. 2003, MNRAS, 238, 465
Asensio Ramos, A., Martínez González, M. J., & Rubiño-Martín, J. A. 2007, A&A, 476, 959
Athanassoula, E. 1980, A&A, 88, 184
Athanassoula, E. 1992, MNRAS, 259, 328
Athanassoula, E., & Misiriotis, A. 2002, MNRAS, 330, 35
Bakos, J., Trujillo, I., & Pohlen, M. 2008, ApJ, 683, L103
Beckman, J. E., Varela, A. M., Muñoz-Tuñón, C., Vilchez, J. M., & Cepa, J. 1991, A&A, 245, 436
Bell, E. F., McIntosh, D. H., Katz, N., & Weinberg, M. D. 2003, ApJS, 149, 289
Bianchi, L., et al. 2003a, in The Local Group as an Astrophysical Laboratory, ed. M. Livio & T. Brown (Baltimore, MD: STScI), 10
Bianchi, L., et al. 2003b, BAAS, 35, 1354
Binney, J., & Tremaine, S. 1987, Galactic dynamics (Princeton, NJ: Princeton Univ. Press)
Bland-Hawthorn, J., Vlajić, M., Freeman, K. C., & Draine, B. T. 2005, ApJ, 629, 239
Boissier, S., et al. 2007, ApJS, 173, 524
Bosma, A., van der Hulst, J. M., & Sullivan, W. T., III. 1977, A&A, 57, 373
Bournaud, F., Elmegreen, B. G., & Elmegreen, D. M. 2007, ApJ, 670, 237
Braun, R. 1995, A&AS, 114, 409
Buta, R. 1988, ApJS, 66, 233
Buta, R. J., Corwin, H. G., Jr., & Odewahn, S. C. 2007, in The de Vaucouleurs Atlas of Galaxies (Cambridge: Cambridge Univ. Press)
Buat, V., et al. 2005, ApJ, 619, L51
Cho, J., & Park, C. 2009, ApJ, 693, 1045
Dale, D. A., et al. 2007, ApJ, 655, 863
Davies, E. 1990, Machine Vision: Theory, Algorithms and Practicalities (New York: Elsevier)
de Blok, W. J. G., Walter, F., Brinks, E., Trachternach, C., Oh, S.-H., & Kennicutt, R. C. 2008, AJ, 136, 2648
de Vaucouleurs, G., de Vaucoleurs, A., Corwin, H. G., Jr., Buta, R. J., Paturel, G., & Fouqué, P. 1991, Third Reference Catalogue of Bright Galaxies (New York: Springer)
Debattista, V. P., Mayer, L., Carollo, C. M., Moore, B., Wadsley, J., & Quinn, T. 2006, ApJ, 645, 209
Donas, J., Milliard, B., Laget, M., & Deharveng, J. M. 1981, A&A, 97, L7
Elmegreen, B. G., & Hunter, D. A. 2006, ApJ, 363, 712
Elmegreen, B. G., & Parravano, A. 1994, ApJ, 435, L121
Erwin, P. 2004, A&A, 415, 941
Erwin, P., Beckman, J. E., & Pohlen, M. 2005, ApJ, 626, L81
Erwin, P., Pohlen, M., & Beckman, J. E. 2008a, AJ, 135, 20
Erwin, P., Pohlen, M., Gutierrez, L., & Beckman, J. E. 2008b, in ASP Conf. Ser. 396, Formation and Evolution of Galaxy Disks, ed. J. G. Funes (San Francisco, CA: ASP), 207
Ferguson, A. M. N., & Clarke, C. J. 2001, MNRAS, 325, 781
Ferrers, N. M. 1877, Q. J. Appl. Math., 14, 1
Foyle, K., Courteau, S., & Thacker, R. J. 2008, MNRAS, 386, 1821
Freeman, K. C. 1970, ApJ, 160, 811
Gil de Paz, A., et al. 2004, BAAS, 36, 1410
Gil de Paz, A., et al. 2005, ApJ, 627, L29
Gil de Paz, A., et al. 2007, ApJS, 173, 185
Haralick, R., & Shapiro, L. 1992, Computer and Robot Vision (Vol. 1; Reading, MA: Addison-Wesley Publishing Company)
Heller, C. H., & Shlosman, I. 1994, ApJ, 424, 84
Hopkins, P. F., Cox, T. J., Younger, J. D., & Hernquist, L. 2009, ApJ, 691, 1168
Hunter, D. A., & Elmegreen, B. G. 2006, ApJS, 162, 49
Jarrett, T. H., Chester, T., Cutri, R., Schneider, S., & Huchra, J. P. 2003, AJ, 125, 525
Jogee, S., Knapen, J. H., Laine, S., Shlosman, I., Scoville, N. Z., & Englmaier, P. 2002, ApJ, 570, L55
Karachentsev, I. D. 2005, AJ, 129, 178
Karachentsev, I. D., et al. 2003, A&A, 398, 467
Kazantzidis, S., Bullock, J. S., Zentner, A. R., Kravtsov, A. V., & Moustakas, L. A. 2008, ApJ, 688, 254

Kennicutt, R. C. 1989, ApJ, 344, 685
Kennicutt, R. C. 1998, ARA&A, 36, 189
Kennicutt, R. C., et al. 2003, PASP, 115, 928
Kormendy, J., & Norman, C. A. 1979, ApJ, 233, 539
Kormendy, J., & Kennicutt, R. C. 2004, ARA&A, 42, 603
Larkin, J. E., Armus, L., Knop, R. A., Soifer, B. T., & Matthews, K. 1998, ApJS, 114, 59
Lindblad, P. 0. 1960, Stockkholms Obs. Ann., 21, 4
Maoz, D., Filippenko, A. V., Ho, L. C., Rix, H.-W., Bahcall, J. N., Schneider, D. P., & Macchetto, F. D. 1995, ApJ, 440, 91
Martin, D. C., et al. 2005, ApJ, 619, L1
Martínez-Delgado, D., Peñarrubia, J., Gabany, R. J., Trujillo, I., Majewski, S. R., & Pohlen, M. 2008, ApJ, 689, 184
Martinez-Valpuesta, I., Shlosman, I., & Heller, C. H. 2006, ApJ, 637, 214
Metropolis, N., Rosenbluth, A. W., Rosenbluth, M. N., Teller, A. H., & Teller, E. 1953, J. Chem. Phys., 21, 1087
Miyamoto, M., & Nagai, R. 1975, PASJ, 27, 533
Möllenhoff, C., Matthias, M., & Gerhard, O. E. 1995, A&A, 301, 359
Mulder, P. S. 1995, A&A, 303, 57
Mulder, P. S., & Combes, F. 1996, A&A, 313, 723
Muñoz-Mateos, J. C., Gil de Paz, A., Boissier, S., Zamorano, J., Jarrett, T., Gallego, J., & Madore, B. F. 2007, ApJ, 658, 1006
Muñoz-Tuñón, C., Prieto, M., Beckman, J. E., & Cepa, J. 1989, Ap&SS, 156, 301
Neal, R. M. 1993, Probabilistic Inference Using Markov Chain Monte Carlo Methods (Technical Report No. 0506; Toronto: Dept. of Statistics, University of Toronto)
Panuzzo, P., et al. 2007, ApJ, 656, 206
Papayannopoulos, T., & Petrou, M. 1983, A&A, 119, 21
Patsis, P. A. 2005, MNRAS, 358, 305
Peñarrubia, J., McConnachie, A., & Babul, A. 2006, ApJ, 650, L33
Pohlen, M., Dettmar, R.-J., Lütticke, R., & Aronica, G. 2002, A&A, 392, 807
Pohlen, M., & Trujillo, I. 2006, A&A, 454, 759
Roberts, T. P., Schurch, N. J., & Warwick, R. S. 2001, MNRAS, 324, 737
Roberts, T. P., Warwick, R. S., & Ohashi, T. 1999, MNRAS, 304, 52
Romero-Gómez, M., Athanassoula, E., Masdemont, J. J., & García-Gómez, C. 2007, A&A, 472, 63
Roškar, R., Debattista, V. P., Stinson, G. S., Quinn, T. R., Kaufmann, T., & Wadsley, J. 2008, ApJ, 675, L65
Salpeter, E. E. 1955, ApJ, 121, 161
Sanders, R. H., & Huntley, J. M. 1976, ApJ, 209, 53
Sanders, R. H., & Tubbs, A. D. 1980, ApJ, 235, 803
Shaw, M. A., Combes, F., Axon, D. J., & Wrigth, G. S. 1993, A&A, 273, 31
Schaye, J. 2004, ApJ, 609, 667
Schlegel, D. J., Finkbeiner, D. P., & Davis, M. 1998, ApJ, 500, 525
Schwarz, M. P. 1985, MNRAS, 212, 677
Silva, L., Granato, G. L., Bressan, A., & Danese, L. 1998, ApJ, 509, 103
Smith, B. J., Harvey, P. M., Colomé, C., Zhang, C. Y., DiFrancesco, J., & Pogge, R. W. 1994, ApJ, 425, 91
Smith, B. J., Lester, D. F., Harvey, P. M., & Pogge, R. W. 1991, ApJ, 373, 66
Slyz, A. D., Devriendt, J. E. G., Silk, J., & Burkert, A. 2002, MNRAS, 333, 894
Sofue, Y., Tutui, Y., Honma, M., Tomita, A., Takamiya, T., Koda, J., & Takeda, Y. 1999, ApJ, 523, 136
Taniguchi, Y., Ohyama, Y., Yameda, T., Mouti, H., & Yoshida, M. 1996, ApJ, 467, 215
Thilker, D. A., et al. 2005, ApJ, 619, L79
Toomre, A. 1969, ApJ, 158, 899
Turner, J. L., & Ho, P. T. P. 1994, ApJ, 421, 122
van den Bosch, F. C. 2001, MNRAS, 327, 1334
van der Kruit, P. C. 1976, A&A, 52, 85
van der Kruit, P. C. 1979, A&AS, 38, 15
van der Kruit, P. C. 1987, A&A, 173, 59
van der Kruit, P. C., & Searle, L. 1981a, A&A, 95, 105
van der Kruit, P. C., & Searle, L. 1981b, A&A, 95, 116
Velázquez, H., & White, S. D. M. 1999, MNRAS, 304, 254
Waller, W. H., et al. 2001, AJ, 121, 1395
Walter, F., Brinks, E., de Blok, W. J. G., Bigiel, F., Kennicutt, R. C., Thornley, M. D., & Leroy, A. 2008, AJ, 136, 2563
York, D. G., et al. 2000, AJ, 120, 1579
Yoshii, Y., & Sommer-Larsen, J. 1989, MNRAS, 236, 779
Younger, J. D., Besla, G., Cox, T. J., Hernquist, L., Robertson, B., & Willman, B. 2008, ApJ, 676, L21
Younger, J. D., Cox, T. J., Seth, A. C., & Hernquist, L. 2007, ApJ, 670, 269